JOURNAL OF THE ROYAL SOCIETY Interface

rsif.royalsocietypublishing.org

Research

Cite this article: Ramananarivo S, Godoy-Diana R, Thiria B. 2013 Passive elastic mechanism to mimic fish-muscle action in anguilliform swimming. J R Soc Interface 10: 20130667.
http://dx.doi.org/10.1098/rsif.2013.0667

Received: 23 July 2013
Accepted: 2 August 2013

Subject Areas:
bioengineering, biomechanics, biomimetics

Keywords:
fluid–structure interaction, anguilliform swimming, slender body

Author for correspondence:
Sophie Ramananarivo
e-mail: sophie.ramananarivo@espci.fr

Electronic supplementary material is available at http://dx.doi.org/10.1098/rsif.2013.0667 or via http://rsif.royalsocietypublishing.org.

Royal Society Publishing
Informing the science of the future

Passive elastic mechanism to mimic fish-muscle action in anguilliform swimming

Sophie Ramananarivo, Ramiro Godoy-Diana and Benjamin Thiria

Physique et Mécanique des Milieux Hetérogènes (PMMH), CNRS UMR 7636, ESPCI ParisTech, UPMC (Paris 6), Université Paris Diderot (Paris 7), 10 rue Vauquelin, 75231 Paris, Cedex 5, France

Swimmers in nature use body undulations to generate propulsive and manoeuvring forces. The anguilliform kinematics is driven by muscular actions all along the body, involving a complex temporal and spatial coordination of all the local actuations. Such swimming kinematics can be reproduced artificially, in a simpler way, by using the elasticity of the body passively. Here, we present experiments on self-propelled elastic swimmers at a free surface in the inertial regime. By addressing the fluid–structure interaction problem of anguilliform swimming, we show that our artificial swimmers are well described by coupling a beam theory with the potential flow model of Lighthill. In particular, we show that the propagative nature of the elastic wave producing the propulsive force is strongly dependent on the dissipation of energy along the body of the swimmer.

1. Introduction

Undulatory propulsion is a means of locomotion shared by living organisms over a wide range of scales and in many different media [1]. From snakes [2] to sandfish [3], from eels [4] to spermatozoa or motile bacteria [5], net forward motion is achieved by propagating waves along a deformable body. In fluids, the anguilliform swimming dynamics was first addressed in pioneering studies during the 1950s and 1960s by Taylor [6], Gray & Hancock [7], Machin [8] and Lighthill [9]. They established that the propulsive force originates from either viscous friction (the so-called *resistive* theory) or inertial momentum transfer (Lighthill's *reactive* model), depending on the regime of Reynolds number, which measures the importance of inertial to viscous actions in a given flow. In both cases, the characteristics of the propagating wave (phase velocity, wavelength and amplitude) are crucial in determining the swimming performance [9,10].

A vast amount of theoretical and numerical works has followed [10–14], from Stokes or viscoelastic flows related to microorganism propulsion [5] to inertial regimes [15,16] or three-dimensional geometries [17]. This research shed light on various undulatory swimming modes, and not only provided the basis for a broad spectrum of applications in robotics and engineering at the macroscale, but also in the public health domain where, for instance, sperm swimming speed is significantly related to fertilization success [18].

In the inertial regime, the most relevant analytical model of fish swimming is Lighthill's reactive theory. Based on a potential flow approximation, Lighthill showed that the estimation of the thrust force requires only the knowledge of the local kinematics at the tail of the deformable body [10]. Thus, calling y, the local deflection of the slender body with respect to the axis of swimming (x-axis), and U the swimming velocity, the average total thrust force, $\langle T\rangle$, reduces, in the limit of small lateral displacement, to

$$\langle T\rangle = \frac{1}{2}\rho S[\langle(\partial_t y)^2\rangle - U^2\langle(\partial_x y)^2\rangle]_r, \tag{1.1}$$

where ρS is the added mass of fluid (with ρ the fluid density and S the swimmer cross section). The subscript r refers to the location of the tail where $\partial_x y$ and $\partial_t y$ are estimated. This expression of the force is obtained writing that the swimming power $\langle T\rangle U$ (i.e. the product of the thrust force times the swimming velocity) corresponds to the rate of working done by the fish, $\langle W\rangle$, minus the

rate of shedding of the kinetic energy associated with lateral fluid motion, say $\langle T\rangle U = \langle W\rangle - 1/2\rho S\langle(\partial_t y + U\partial_x y)_r^2\rangle U$. The part corresponding to the energy transferred to the fluid can be seen as a source of dissipation for the mechanics of the swimming fish, as this energy is lost into the flow. In the case of passive swimmers that rely on elasticity to propagate the undulating motion, this dissipated energy will not be available to sustain the body deformation (see [19] in the context of energy harvesting). The value of the thrust force depends thus on the nature of the near- body flow field, which is extensively discussed in this work.

For living animals, the kinematics of the propagating wave is obtained by local contractions of the muscles all along the body. The phase velocity, wavelength and wave amplitude are therefore set separately in order to select a specific regime. However, in the case of artificial mimics of real swimmers, a mechanical model of fish-muscle action would require a continuous distribution of actuators [20]. Such a design is not only complicated, but also difficult to scale down in size. Another approach is to consider a local actuation and use the elasticity of the body to propagate the wave [16,21–23]. The implementation of the forcing that will provide the necessary energy to create the anguilliform kinematics is therefore much simplified.

Here, we present a full description of the mechanics of such self-propelled swimmers using a careful experimental set-up and solving the complete fluid–structure problem of a forced beam in a fluid in the inertial regime. The challenge in the latter is to obtain an estimation of the tail kinematics as a function of the forcing, using a coupled fluid–elasticity approach. The average swimming velocity, along with an estimation of the swimming efficiency, is predicted afterwards by balancing the thrust from Lighthill's prediction and the drag force. We also address the more general problem of wave propagation in bounded media, using a local energy injection. The dynamics of the propagating wave that drives the anguilliform locomotion is shown, in particular, to have a crucial dependence on energy dissipation along the body of the swimmer. Furthermore, we show that in the inertial regime, self-propelled swimmers using passive elastic deformation verify Lighthill's reactive theory even at a free surface. From this work, we confirm the potential of the present experiment to be of importance in the future design of artificial swimmers.

2. Results

2.1. Swimming kinematics

The slender swimmer in the present experiment is actuated on one extremity using magnetic interactions. The induced motion of the head is a combination of heaving and pitching, and the resulting body undulations propel the filament on the surface of a water tank (see figure 1 and Material and methods for details).

The present system differs from Lighthill's configuration in that the swimmer is not fully immersed in the fluid (it is placed at the air–water interface to confine its displacements into a two-dimensional plane). In particular, surface waves generated by the moving cylinder radiate energy away from it and may represent an extra source of drag [24–26]. However, this so-called wave drag can be neglected here as the ratio of the wave drag to form drag, proportional to the square of the Weber number [27], remains small (10^{-6} to 0.1).

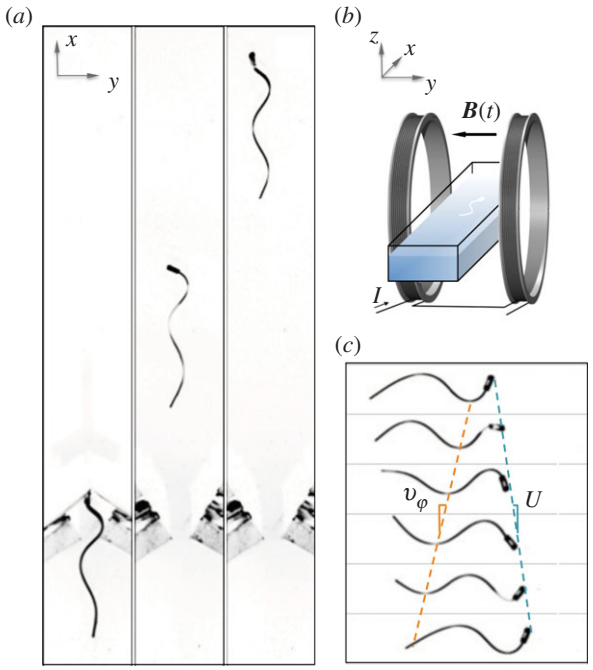

Figure 1. Experimental set-up: (*a*) Top-view snapshots of the swimmer propelling itself forward after the opening of the gates (that are visible at the bottom of the images). (See the electronic supplementary materials, movie S1, seeding particles have been added on the surface to visualize the flow.) (*b*) Swimmer at the free surface of a water tank consisting of a flexible cylindrical tail made of acrylic polymer. A magnet embedded in the head of the filament is forced to oscillate using the time-varying magnetic field produced by a Helmholtz pair. (*c*) Successive pictures of a filament over a period of undulation showing the forward swimming velocity, U, and the speed of the travelling wave, v_φ.

We vary the length of the swimmer, L, and the frequency of the sinusoidal forcing, f, while the other parameters are kept constant for simplicity (among them, the amplitude of the prescribed displacement at the head, A_f, and the flexural rigidity of the body, B). The full kinematics of the swimmer as a function of the experimental parameters is recovered from high-speed camera recordings. From this, we extract the time evolution of the local deflection $y(s, t)$ (where s is the local curvilinear abscissa along the centreline of the body), the wave speed v_φ, and the cruising velocity U (figure 1).

The results are plotted in figure 2. Figure 2*a* shows the evolution of the cruising velocity as a function of the beat frequency for different lengths of the swimmer. U is found to be an increasing function of the forcing frequency for all the swimmers tested. It can also be seen that 'short' swimmers are faster than 'long' swimmers in the range of parameters tested. This can be understood by considering the results displayed in figure 2*b*: for a given forcing amplitude and forcing frequency (A_f, f), the tail amplitude, A_r, is decreasing with L. As thrust is based on the kinematics at the tail, and consequently on A_r, short swimmers will therefore swim faster. More generally, as illustrated in figure 2*f*, the overall shape of the swimmers tends to decrease in amplitude along the length. This characteristic shape is of course highly dependent on the forcing parameters and the length of the swimmer and is owing to the fact that the energy is not conserved along the body. A further crucial information for the swimming efficiency [9] that can be extracted from the kinematics of the undulating filament is the phase velocity, v_φ, which is displayed in the inset in figure 2*d*. A first observation is that, as

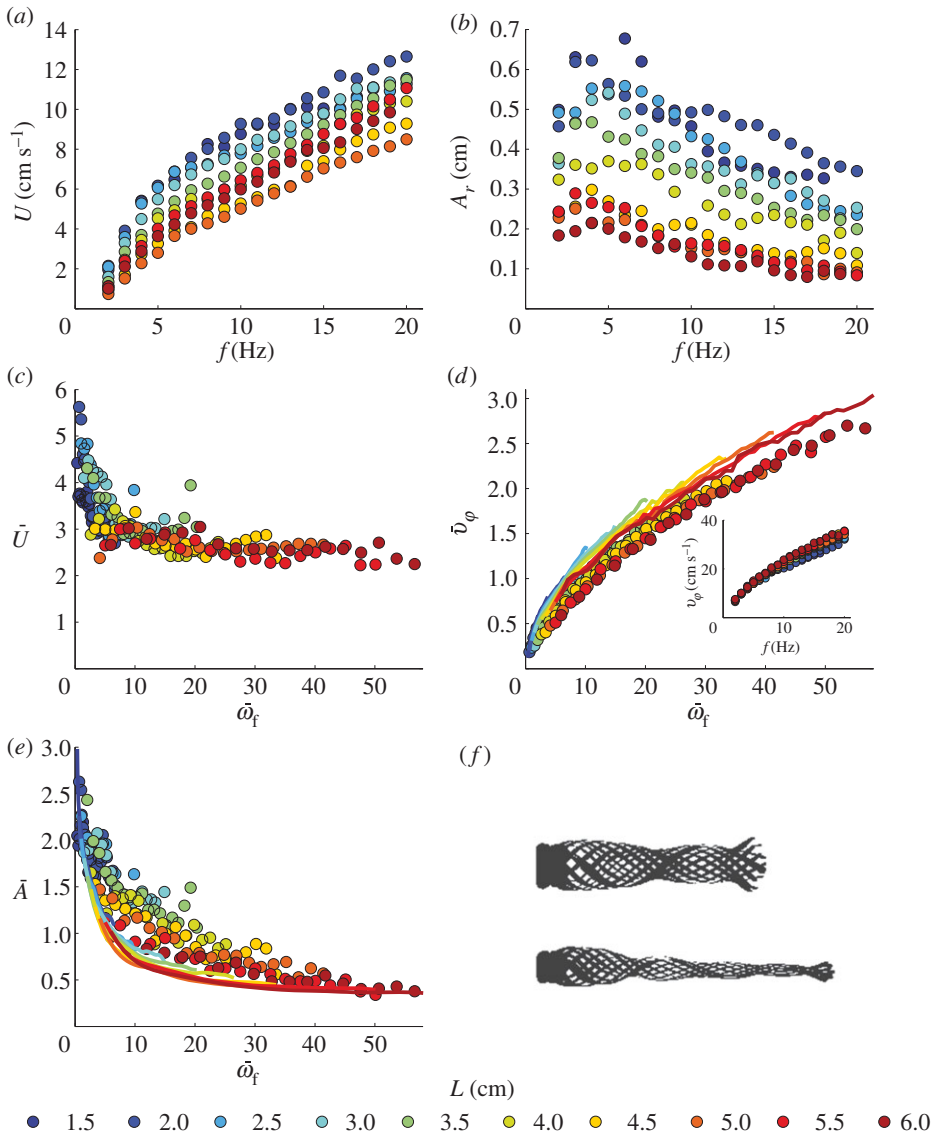

Figure 2. (*a*) Swimming velocity, (*b*) amplitude of the oscillations at the tail and (inset in *d*) phase velocity, as a function of the forcing frequency. Experimental data plotted in a non-dimensionalized form, as a function of the non-dimensionalized angular frequency $\bar{\omega}_f = \omega_f/\omega_0$, with $\omega_0 = (2\pi/L^2)(B/(\mu+\rho S))^{1/2}$: (*c*) ratio of the cruising velocity and the characteristic actuation speed $\bar{U} = U/fA_f$, (*d*) non-dimensionalized phase velocity $\bar{v}_\varphi = v_\varphi/\omega_0 L$, (*e*) amplitude of the oscillation at the tail normalized by that of the head $\bar{A} = A_r/A_f$. The solid lines correspond to the theoretical predictions of the model presented in the 'Fluid–structure model' section. (*f*) Typical undamped (3 cm long filament forced at 10 Hz) and damped (4 cm long filament forced at 20 Hz) amplitude envelopes (see the electronic supplementary material, movieS2 and S3).

expected, the global behaviour is independent of the length of the filament.

All the experimental observations can be collapsed by plotting the data in a compact form using the characteristic lengths and velocities of our system. We define ω_0 as the natural relaxation frequency of the elastic filament: $\omega_0 = (2\pi/L^2)(B/(\mu+\rho S))^{1/2}$, with μ its mass per unit length. Figure 2*c–e* displays, respectively, the non-dimensionalized swimming velocity $\bar{U} = U/fA_f$, phase velocity $\bar{v}_\varphi = v_\varphi/\omega_0 L$ and amplitude $\bar{A} = A_r/A_f$, as a function of $\bar{\omega}_f = \omega_f/\omega_0$, where $\bar{\omega}_f = 2\pi f$ denotes the angular frequency. Note that $\bar{U}$ has the same form as the inverse of the Strouhal number, as defined in the context of self-propelled swimmers (e.g. [20,28]). $\bar{U}$, which compares the characteristic speed of the imposed head oscillations to the cruising speed, decreases and converges to an asymptotic value. Its decay has to be compared and correlated with the decrease of $\bar{A}$ with $\bar{\omega}_f$, that is a consequence of passive elastic propagation.

2.2. Fluid–structure model

In the following section, we aim to understand the mechanisms involved in the motion of the filament, to be able to predict what would be the output from a given forcing, and conversely what would be the required forcing to achieve a given kinematics. The filament is modelled as a forced slender beam [29] of length L with circular cross section $S = \pi d^2/4$ (with d its diameter), mass per unit length μ and stiffness B. It is immersed in a uniform fluid of density ρ, moving at velocity U. We neglect, in the present model, any effect of the interface by considering a filament moving in the bulk. The beam obeys the Euler–Bernouilli equation

$$\mu\partial_t^2\mathbf{r} + B\partial_s^4\mathbf{r} - \partial_s(T\partial_s\mathbf{r}) + f\,\hat{\mathbf{n}} = 0, \qquad (2.1)$$

with s the curvilinear coordinate, $\mathbf{r}(s,t) = (x,y)$ the beam position, f the fluid forces acting on the beam, T, a tension in the plate that enforces the inextensibility condition

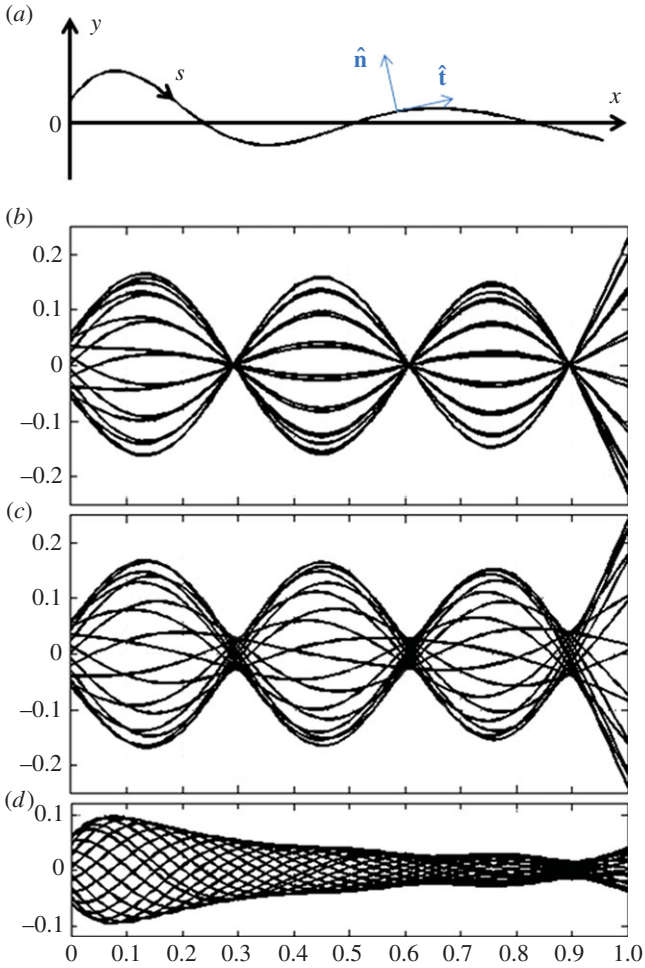

Figure 3. (*a*) Definition of the coordinates and geometry of the beam model considered. Simulated motion of the beam when implementing equation (2.7) gradually: (*b*) with only the two first terms describing a classic elastic beam (*c*) adding the 'flag' terms in brackets, (*d*) adding the quadratic fluid term. (Online version in colour.)

$\|\partial_s \mathbf{r}\| = 1$ and $\hat{\mathbf{n}}$ the unit vector normal to the beam (figure 3*a*). The extremity of the beam in $s = L$ is free, that is $\partial_s^3 y(L,t) = \partial_s^2 y(L,t) = 0$. The head of the filament ($s = 0$) is actuated with a prescribed periodic displacement and rotation: $y(0,t) = A_f \cos(\omega_f t)$, $\partial_x y(0,\ t) = \theta_f \cos(\omega_f t + \phi)$, with ω_f the angular frequency, θ_f the maximal rotation angle of the head and ϕ the phase shift between pitching and heaving (see also [30]).

In the limit of slender structures ($d/L \ll 1$), and for purely potential flow, Lighthill provided a leading order expression of the fluid force acting on the beam [31]. This so-called *reactive* force results from the reaction of the fluid accelerated by the body movements and can be expressed as [32,33]

$$f_r = -M(\partial_t u_n - \partial_s(u_n u_t) + \frac{1}{2}u_n^2 \kappa), \tag{2.2}$$

where $M = \rho S$ is the added mass per unit length owing to the fluid, κ is the beam curvature, u_t and u_n are the longitudinal and normal components of the beam velocity, respectively, relative to the uniform water flow (so that $\partial_t \mathbf{r} - \mathbf{U} = u_t \hat{\mathbf{t}} + u_n \hat{\mathbf{n}}$, with $\hat{\mathbf{t}} = \partial \mathbf{r}/\partial s$ the unit vector tangent to the filament). Another contribution for the fluid force is added to account for the loss of energy along the swimmer. Considering that the transverse Reynolds numbers encountered

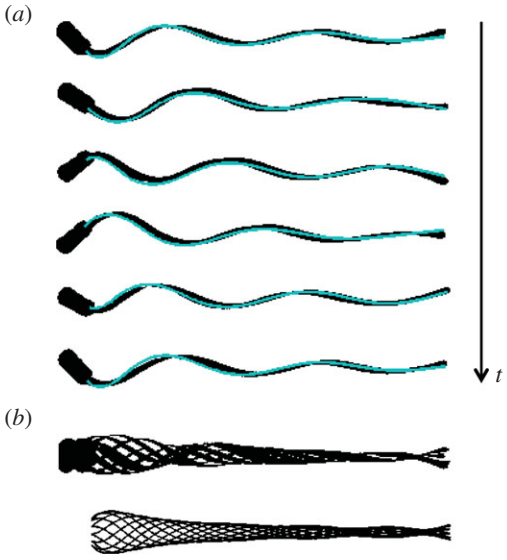

Figure 4. (*a*) Successive computed shapes superimposed to pictures of a 4.5 cm long swimmer forced at $f = 19$ Hz and (*b*) the corresponding experimental and theoretical amplitude envelopes. (Online version in colour.)

in the present experiment are $Re_t = A_f\ \omega_f\ d/\nu \approx 10$–$140$, this term is given the classic quadratic form (e.g. [6,34,35])

$$f_d = -\frac{1}{2}\rho d C_d |u_n| u_n, \tag{2.3}$$

with C_d the drag coefficient associated to transverse motions.

Inserting $f = f_r + f_d$ into equation (2.1) and projecting the equation on the x- and y-axes gives two coupled dynamical equations for $x(s,t)$ and $y(s,t)$. Following Eloy *et al.* [33], the equations are decoupled by first using the x-projection to evaluate the tension T, and then eliminating $x(s,t)$ and its derivatives using the inextensibility condition (see also [36]). We assume that the lateral deflections are small ($y \ll L$ and $\partial_s y \ll 1$) and discard the terms of order larger than y^2. The curvilinear coordinate s is approximated by its abscissa x, the first corrections coming up through this substitution being of order y^3. This yields the weakly nonlinear dynamical equation

$$\mu \partial_t^2 y + B \partial_x^4 y - f_r - f_d + O(y^3) = 0, \tag{2.4}$$

with

$$f_r = -M(\partial_t^2 y + 2U\partial_t \partial_x y + U^2 \partial_x^2 y) + O(y^3) \tag{2.5}$$

and

$$f_d = -\frac{1}{2}\rho d C_d |\partial_t y + U\partial_x y|(\partial_t y + U\partial_x y). \tag{2.6}$$

Equation (2.4) is non-dimensionalized using L and $L^2\sqrt{\mu/B}$ as characteristic length and time. It reads

$$\begin{aligned}(1+\tilde{m})\partial_{\tilde{t}}^2 \tilde{y} + \partial_{\tilde{x}}^4 \tilde{y} + \tilde{m}[2\tilde{U}\partial_{\tilde{t}}\partial_{\tilde{x}}\tilde{y} + \tilde{U}^2\partial_{\tilde{x}}^2\tilde{y}] \\ +\tilde{\alpha}|\partial_{\tilde{t}}\tilde{y} + \tilde{U}\partial_{\tilde{x}}\tilde{y}|(\partial_{\tilde{t}}\tilde{y} + \tilde{U}\partial_{\tilde{x}}\tilde{y}) = 0.\end{aligned} \tag{2.7}$$

The dimensionless quantities are noted with tildes; $\tilde{U} = UL\sqrt{\mu/B}$ is the reduced velocity, $\tilde{m} = M/\mu$ the mass ratio and $\tilde{\alpha} = \frac{1}{2}\rho d C_d L/\mu$ the non-dimensionalized damping coefficient. Note that $\tilde{\alpha}$ depends on L, which reflects the increasing effect of damping when the filament is longer. Equation (2.7) is solved numerically (see Material and methods) using the experimental parameters. Here, the only unknown parameter is the transverse drag coefficient C_d. It is determined using a minimization approach (see Material and methods). Figure 4 shows the experimental and

computed time dynamics of a 4.5 cm long filament, using the obtained value of C_d.

The first two terms of equation (2.7) are the classic ingredients of the beam equation: the inertia of the beam (with an added mass effect owing to the surrounding fluid), balanced by an elastic restoring force. The action of the fluid brings two additional effects: a quadratic dissipation term (last term) and a 'flag' term (in square braquets) which depends on the swimming velocity U. The flag term is known to cause the beam to flutter above a critical flow velocity (this is called the flapping-flag instability, e.g. [29,37–39]). In the range of parameters of the experiments ($\tilde{m} \approx 0.96$, $\tilde{U} \in [0.2 - 4]$ and $\tilde{\alpha} \in [50 - 150]$), the dissipative part has an order of magnitude 10–30 times greater than the other dimensionless fluid term, which makes it the main fluid contribution in the dynamical balance.

Interestingly, in our system, this term is also responsible for the wave propagation along the beam, a specific feature of anguilliform swimming; this is a non-trivial question as such bounded elastic systems usually produce, by definition, standing waves. Indeed, the implementation of the first two terms describing the elastic beam (i.e. without any losses in transmission) yields a stationary wave (figure 3*b*). When adding the 'flag' term, the obtained kinematics slightly departs from a standing wave, but the velocities reached by the swimmers are not sufficient to trigger propagation (figure 3*c*). The flag forces related to the upstream velocity U have thus a minor effect on the mechanism of propagation, because our range of parameters lies below the onset of the flapping [40]. This assertion is supported by the fact that, experimentally, the kinematics of the filament is similar when swimming behind the gates ($U = 0$) and when moving freely at its cruising velocity along the water tank (see the electronic supplementary materials, movie S1). However, including the quadratic fluid force does enable propagation by drawing enough energy from the beam to prevent the build-up of a standing wave (figure 3*d*). This dissipative action of the surrounding fluid is thus decisive, in that it allows the undulations to develop into a travelling wave.

It is important to note that, physically, the quadratic term in equation (2.3) reflects the kinetic energy lost into the fluid through transverse flow separation at each half-stroke (e.g. [41]). In Lighthill's theory, the estimation of the thrust generated by the swimmer is based on considerations of momentum and energy losses [9]. Our system differs from this theory in that, energy is not only wasted from the tail, but also from the sides. Dissipation thus contributes to the energy balance through an additional wasted kinetic energy term that can be written in a similar way to the kinetic energy lost in the wake. The available energy to produce thrust is hence reduced, but the global mechanism for propulsion remains unchanged. At first approximation, the expression of the thrust, taking into account quadratic dissipation, has the form given by equation (1.1) but with a correction factor depending on the transverse drag coefficient C_d. For the determination of the cruising velocity and the swimming efficiency, this correction is taken into account when balancing the expression of the thrust force with the global drag of the swimmer, through the adjustable coefficient C_D. Transverse flow separation impacts the performance of the swimmer mostly by damping the body oscillations along its length (owing to the fact that energy is extracted from the solid and transferred univocally to the fluid).

The results of the numerical simulation are plotted in figure 2 in solid lines. The phase velocity is computed *a posteriori* from the simulated motion of the beam. The measurement is performed in the same way as for experimental data, by tracking in time, the position of the points of the swimmer crossing the body midline. Comparison between experimental data and theoretical predictions shows a good agreement, with a relative deviation of 22% for $\bar{v}_\varphi$ and 29% for $\bar{A}$. This confirms the ability of the present model to describe our system and to predict the tail amplitude as well as the phase velocity.

One should note that, despite the possible surface effects mentioned previously, the model of a fully immersed swimmer described by equation (2.7) provides a good prediction of the time–space dynamics of our surface swimmer. This leads to the conclusion that surface effects may either be negligible or already incorporated in the adjustable quadratic fluid dissipation term (equation (2.3)). A detailed study of the surface deformations is the subject of ongoing work.

3. Discussion

3.1. Swimming speed

Using Lighthill's model (equation (1.1)), we obtain a prediction for the thrust force. The swimming speed reached in the steady-state regime is then determined by a balance between the thrust generated and the drag experienced by the filament. In the regimes encountered here, the swimmer produces a significant wake whose width is set by the amplitude of the tail displacement A_r; the drag is hence given the form [41]

$$\langle D \rangle = \frac{1}{2}\rho U^2 C_D S', \tag{3.1}$$

where C_D is a drag coefficient and $S' = 2A_r \times d$ the effective section. Using a simplified kinematics $y(x,t) = A_r \cos(2\pi(ft - x/\lambda))$ (with λ, the wavelength), the equality between equations (1.1) and (3.1) gives us a first-order estimation of the swimming velocity

$$U = \Gamma(\lambda, A_r) v_\varphi, \tag{3.2}$$

where $\Gamma(\lambda, A_r) = (1 + S' C_D \lambda^2 / 2 S A_r^2 \pi^2)^{-1/2}$ is a function of the spatial shape characteristics of the swimmer. Although desirable, a robust measurement or prediction of C_D for a slender structure whose shape is changing in time is very difficult to perform, especially as the nature of this drag is not a straightforward question.[1] In the following, it has been used as an adjustable parameter and its value of $C_D \approx 0.23$ is in agreement with the order of magnitude of the drag coefficient of streamlined bodies [42].

All data points from the present experiments are plotted in the compact form of equation (3.2) in figure 5*a*. It is noteworthy that, although the theory is based on relatively simple arguments, the data collapse around a single linear relationship. A slight deviation above the master curve is observed for the longest filaments, meaning that the obtained value of $C_D \approx 0.23$ overestimates the actual drag. This may be related to the enhanced streamlining of the envelope of oscillation observed for long filaments where the amplitude at the tail A_r is significantly smaller than that of the head.

The estimate of U provided by Lighthill's theory completes the beam model introduced previously in characterizing our swimmer.

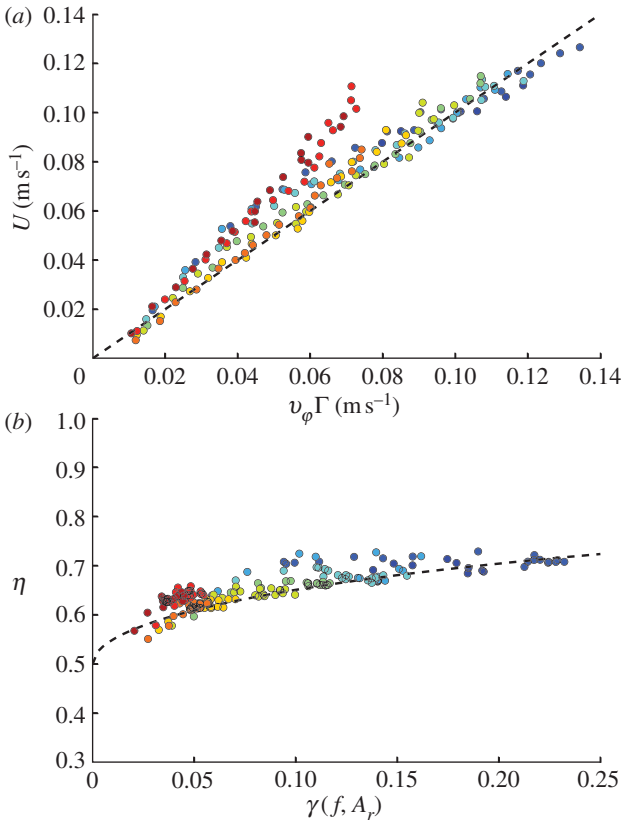

Figure 5. (*a*) Implementation of equation (3.2) using experimental data. The line of slope unity around which the data line up is the identity defined by Lighthill's theory. A single value of $C_D \approx 0.23$ was used, which is obtained as an adjustable parameter giving the best fit of all points. (*b*) Hydromechanical efficiency, calculated from equation (3.3), plotted against γ which is a function of the kinematic characteristics of the swimmer. The dotted line corresponds to the $\eta(\gamma) = 1/2(1 + \sqrt{\gamma/(1+\gamma)})$ function issued from Lighthill's theory.

3.2. Efficiency

Following Lighthill's steps, one can then define an efficiency (similar to the Froude efficiency of a propeller), $\eta = U\langle T\rangle/\langle W\rangle$ that illustrates the ability of the swimmer to convert the work done by its flexural movements into useful thrust. When the undulation takes the form of a travelling wave of velocity v_φ, this hydromechanical efficiency can be written (see [10])

$$\eta = 1 - \frac{1}{2}(v_\varphi - U)/v_\varphi. \tag{3.3}$$

In other words, the swimming speed U should tend toward v_φ to produce thrust efficiently; U cannot be too close to v_φ though, or the thrust generated will not be sufficient to overcome the drag resistance $\langle D\rangle$ (the limit case $U = v_\varphi$ corresponding to a swimmer slipping into the water without giving it any lateral displacement). Using equation (3.2), η can be expressed as a function of the kinematic characteristics of the swimmer:

$$\eta = \tfrac{1}{2}\left(1 + \sqrt{\frac{\gamma(\lambda, A_r)}{1+\gamma(\lambda, A_r)}}\right), \tag{3.4}$$

where $\gamma(\lambda, A_r) = \pi^3 dA_r/4C_D\lambda^2$. The efficiency, calculated from equation (3.3), is plotted against γ using experimental data (figure 5*b*). The good agreement with the theoretical γ-function of equation (3.4), represented here by the dotted line, confirms the ability of the expression to describe the dependence of η on λ and A_r. As both lengths result from the elastic response of the filament, equation (3.4) thereby describes how the cost of propulsion changes with the imposed forcing.

In order to make the forcing dependency of the efficiency more explicit and to understand the observed trend in figure 5*b*, $\gamma(\lambda, A_r)$ is rewritten by approximating the dispersion relation to that of a beam immersed in a still fluid without any energy losses, $\lambda = 4\pi^2(B/(\mu + M)^{1/4}f^{-1/2}$. It then reads $\gamma \approx \beta A_r f$, which is homogeneous with respect to the speed of the lateral displacements of the tail, with β a constant set by the characteristics of the fluid–solid system; this γ-form includes both the input (f) and the outcome (A_r) of the 'transfer function' represented by the elastic system. Injecting it into equation (3.4) and noticing that γ is small compared with unity, we get $\eta \approx 1/2(1 + \sqrt{\beta A_r f})$. As observed in figure 5*b*, swimmers thus experience an improved efficiency when increasing the forcing frequency. Note that contrary to swimmers executing standing waves, which cannot achieve efficiencies exceeding 1/2 [9], the present system yields values of η systematically higher than 1/2. This highlights the importance of developing travelling waves along the beam. As mentioned previously, however, passive propagation requires a source of dissipation. This loss of energy causes a decrease in amplitude along the swimmer that is especially pronounced for long filaments or high forcing frequencies (figure 2*f*). In the present experiment, the fact that an increase in frequency cannot be dissociated of a decrease in the amplitude A_r limits the efficiency that can be reached, which consequently is reflected by a saturation in the $\eta(\gamma)$ curve. This limiting effect of the spatial damping also shows in figure 2*c*, where $\bar{U}$ decays with $\bar{\omega}_f$. The crucial question for the present swimmers is then to remove enough energy along the passive elastic body to prevent the build-up of standing waves while maintaining a substantial amplitude of oscillation down to the tail. A key parameter is clearly the magnitude of the dissipative term in equation (2.7), which is quite large in the present experiment, but that will most likely to change for other body shapes or fully submersed swimmers.

4. Conclusions

We have presented useful results for the design of an *easy-to-build* model of a self-propelled swimmer, which could be adapted to other environments and scales. These swimmers differ from fishes in that they are locally actuated and use their elasticity to passively propagate a wave. We fully characterize the swimmer by first developing a model giving a complete description of its dynamics under actuation, and then showing that average swimming speed and efficiency are well predicted by a potential flow theory as introduced by Lighthill.

More precisely, we have shown that the production of anguilliform kinematics is dependent on the ability of the mechanical system to dissipate energy along the body of the swimmer in order to prevent the build-up of stationary waves. In return, this substantial amount of energy lost into the fluid leads to a decrease of the undulations along the length of the swimmer that limits its performance. This non-trivial problem is the focus of oncoming works in relation to previous studies on other passive fluid–elasticity mechanisms relevant to bioinspired propulsion in the inertial

regime [43,44]. Lastly, we have showed that a precise description involves a complete understanding of the nature of the global drag acting against the forward motion. This point will also be studied in near future by taking into account the full kinematics of the swimmer's shape and incorporating viscous effects.

5. Material and methods

5.1. Experiments

The swimmers are composed of a slender cylindrical flexible tail (diameter $d = 460$ µm; flexural rigidity $B = 5.4 \times 10^{-10} \pm 1.0 \times 10^{-10}$ N m^2) made of acrylic polymer (polyvynil syloxane), with a small embedded magnet constituting the head. They float through capillary forces at the free surface of a water tank ($12 \times 6 \times 27$ cm) which is placed between a pair of large coils mounted in a Helmholtz configuration (figure 1*b*). A spatially uniform magnetic field that actuates the head of the swimmer is generated. Applying an AC voltage to the coils produces an oscillating magnetic torque $\mathbf{T}(t) = \mathbf{m} \times \mathbf{B}(t)$ (where $\mathbf{m}$ is the magnetic moment of the magnet and $\mathbf{B}(t)$ is the applied field) as the permanent magnet attempts to align with the alternating field. The rotational oscillations of the magnet generate a backward-propagating wave along the flexible tail, causing it to swim forward. On each run, the swimmer is first held still by a closed gate (figure 1*a*), accelerates from rest when the gate opens and reaches rapidly (in a typical time of order 0.5–1 s) a steady swimming speed U determined by a balance between the forward thrust generated by the body undulations and the drag experienced by the filament. The Reynolds number based on the cruising speed U and the length of the filament L, $Re = UL/\nu$ (ν being the kinematic viscosity of the fluid) ranges from 350 to 6100. Viscous effects are thus negligible with respect to inertia.

5.2. Numerical solution of the fluid–structure model

The motion of the swimmer is assumed to be harmonic, the angular frequency ω_f being set by the forcing, $\tilde{y}(x,t) = Re(\tilde{Y}(x)e^{i\omega_f t})$, where $\tilde{Y}(x)$ is the dimensionless complex amplitude along the beam. We neglected the higher harmonics appearing through the nonlinear term (a time Fourier transform of the body motion showed that they were indeed negligible). Inserting this form of y into equation (2.7) yields the following amplitude equation:

$$-\omega_f^2(1+\tilde{m})\tilde{Y} + \partial_{\tilde{x}}^4\tilde{Y} + \tilde{m}[2i\omega_f\tilde{U}\partial_{\tilde{x}}\tilde{Y} + \tilde{U}^2\partial_{\tilde{x}}^2\tilde{Y}] + \frac{8}{3\pi}\tilde{\alpha}|i\omega_f\tilde{Y} + \tilde{U}\partial_{\tilde{x}}\tilde{Y}|(i\omega_f\tilde{Y} + \tilde{U}\partial_{\tilde{x}}\tilde{Y}) = 0. \quad (5.1)$$

Care needs to be taken with the complex notations for the nonlinear term. The $8/3\pi$ factor comes from the projection of $|\partial_{\tilde{t}}\tilde{y} + \tilde{U}\partial_{\tilde{x}}\tilde{y}|(\partial_{\tilde{t}}\tilde{y} + \tilde{U}\partial_{\tilde{x}}\tilde{y})$ onto the harmonic $e^{i\omega_f t}$ [32]. Equation (5.1) is re-written in a matrix form using finite differences and solved numerically in Matlab to obtain the complex amplitude $\tilde{Y}(x)$, and subsequently the motion of the beam $y(x,t)$. The beam is discretized over 100 points, which is sufficient to account for the spatial variations along its length. The actuation is imposed through the implementation of the boundary conditions.

5.3. Estimation of C_d

We calculated the value of C_d that minimizes the square difference between the simulated and experimental motion (denoted here $y_t(x,t)$ and $y_e(x,t)$) over a time period T, $\int_0^T[\int_0^L(y_t - y_e)^2 dx]^2 dt$. Repeating the process on 27 videos (three different frequencies and nine swimmers of different lengths) yielded mean value $C_d = 2.2 \pm 0.8$, which is consistent with the typical values of order one obtained for bluff bodies [45].

Acknowledgements. We thank Olivier Doaré, Cyril Touzé, Sebastien Michelin, Christophe Eloy and Veronica Raspa for helpful discussions. We also thank Maxime Dana for his help with experimental data and Joseph Tavacoli for his careful reading of the manuscript.

Funding statement. Financial support from the French National Research Agency through project no. ANR-08-BLAN-0099 and of EADS Foundation through project 'Fluids and elasticity in biomimetic propulsion' is gratefully acknowledged.

Endnote

[1]The drag balancing the thrust force could be a combination of form drag and skin friction. Here, form drag is assumed to be dominant, so that we define equation (3.1) with a drag coefficient C_D that is expected to be fairly constant in the range of Reynolds number encountered for this 'bluff body' $Re_b = 2A_rU/\nu \approx [40–10^3]$.

References

1. Gillis GB. 1996 Undulatory locomotion in elongate aquatic vertebrates: anguilliform swimming since Sir James Gray. *Am. Zool.* **36**, 656–665.
2. Graham JB, Lowell WR, Rubinoff I, Motta J. 1987 Surface and subsurface swimming of the sea snake *Pelamis Platurus*. *J. Exp. Biol.* **127**, 27–44.
3. Maladen RD, Ding Y, Li C, Goldman DI. 2009 Undulatory swimming in sand: subsurface locomotion of the sandfish lizard. *Science* **325**, 314–318. (doi:10.1126/science.1172490)
4. Gray J. 1933 Studies in animal locomotion. I. The movement of fish with special reference to the eel. *J. Exp. Biol.* **10**, 88–104.
5. Lauga E, Powers T. 2009 The hydrodynamics of swimming microorganisms. *Rep. Prog. Phys.* **72**, 096601. (doi:10.1088/0034-4885/72/9/096601)
6. Taylor GI. 1952 Analysis of the swimming of long and narrow animals. *Proc. R. Soc. Lond. A* **214**, 158–183. (doi:10.1098/rspa.1952.0159)
7. Gray J, Hancock GJ. 1955 The propulsion of sea-urchin spermatozoa. *J. Exp. Biol.* **32**, 802.
8. Machin KE. 1958 Wave propagation along flagella. *J. Exp. Biol.* **35**, 796–806.
9. Lighthill MJ. 1960 Note on the swimming of slender fish. *J. Fluid Mech.* **9**, 305–317. (doi:10.1017/S0022112060001110)
10. Lighthill MJ. 1970 Aquatic animal propulsion of high hydromechanical efficiency. *J. Fluid Mech.* **44**, 265–301. (doi:10.1017/S0022112070001830)
11. Longman IM, Lavie AM. 1966 On the swimming of a 'Pod'. *IMA J. Appl. Math.* **2**, 273–282. (doi:10.1093/imamat/2.3.273)
12. Lavie AM. 1972 Analysis of the swimming of elastic slender bodies excited by an external force. *J. Fluid Mech.* **53**, 701–714. (doi:10.1017/S0022112072000436)
13. Wu TY. 1971 Hydromechanics of swimming propulsion. I. Swimming of a two-dimensional flexible plate at variable forward speeds in an inviscid fluid. *J. Fluid Mech.* **46**, 337–355. (doi:10.1017/S0022112071000570)
14. Wiggins CH, Goldstein RE. 1998 Flexive and propulsive dynamics of elastica at low Reynolds number. *Phys. Rev. Lett.* **80**, 3879–3882. (doi:10.1103/PhysRevLett.80.3879)
15. Eloy C, Schouveiler L. 2011 Optimisation of twodimensional undulatory swimming at high Reynolds number. *Int. J. Nonlinear Mech.* **46**, 568–576. (doi:10.1016/j.ijnonlinmec.2010.12.007)
16. Alben S, Witt C, Baker TV, Anderson E, Lauder GV. 2012 Dynamics of freely swimming flexible foils. *Phys. Fluids* **24**, 051 901–051 901. (doi:10.1063/1.4709477)
17. Candelier F, Boyer F, Leroyer A. 2011 Threedimensional extension of lighthill's large-amplitude elongated-body theory of fish

locomotion. *J. Fluid Mech.* **674**, 196–226. (doi:10.1017/S002211201000649X)

18. Casselman SJ, Schulte-Hostedde AI, Montgomerie R. 2006 Sperm quality influences male fertilization success in walleye (*Sander vitreus*). *Can. J. Fish. Aquat. Sci.* **63**, 2119–2125. (doi:10.1139/f06-108)
19. Singh K, Michelin S, De Langre E. 2012 The effect of non-uniform damping on flutter in axial flow and energyharvesting strategies. *Proc. R. Soc. A* **468**, 3620–3635. (doi:10.1098/rspa.2012.0145)
20. Triantafyllou MS, Triantafyllou GS, Yue DKP. 2000 Hydrodynamics of fishlike swimming. *Annu. Rev. Fluid Mech.* **32**, 33–53. (doi:10.1146/annurev.fluid.32.1.33)
21. Wiggins CH, Riveline D, Ott A, Goldstein RE. 1998 Trapping and wiggling: elastohydrodynamics of driven microfilaments. *Biophys. J.* **74**, 1043–1060. (doi:10.1016/S0006-3495(98)74029-9)
22. Dreyfus R, Baudry J, Roper ML, Fermigier M, Stone HA, Bibette J. 2005 Microscopic artificial swimmers. *Nature* **437**, 862–865. (doi:10.1038/nature04090)
23. Kósa G, Jakab P, Székely G, Hata N. 2012 MRI driven magnetic microswimmers. *Biomed. Microdevices* **14**, 165–178. (doi:10.1007/S10544-011-9594-7)
24. Raphaël E, De Gennes P-G. 1996 Capillary gravity waves caused by a moving disturbance: wave resistance. *Phys. Rev. E* **53**, 3448–3455. (doi:10.1103/PhysRevE.53.3448)
25. Voise J, Casas J. 2010 The management of fluid and wave resistances by whirligig beetles. *J. R. Soc. Interface* **7**, 343–352. (doi:10.1098/rsif.2009.0210)
26. Benzaquen M, Chevy F, Raphaël E. 2011 Wave resistance for capillary gravity waves: finite-size effects. *Europhys. Lett.* **96**, 34003. (doi:10.1209/0295-5075/96/34003)
27. Bush JWM, Hu DL. 2006 Walking on water: biolocomotion at the interface. *Annu. Rev. Fluid Mech.* **38**, 339–369. (doi:10.1146/annurev.fluid.38.050304.092157)
28. Taylor GK, Nudds RL, Thomas AL. 2003 Flying and swimming animals cruise at a Strouhal number tuned for high power efficiency. *Nature* **425**, 707–711. (doi:10.1038/nature02000)
29. Païdoussis MP. 2004 *Fluid–structure interactions: slender structures and axial flow*. London, UK: Elsevier.
30. Manela A. 2012 Vibration and sound of an elastic wing actuated at its leading edge. *J. Sound Vib.* **331**, 638–650. (doi:10.1016/j.jsv.2011.09.020)
31. Lighthill MJ. 1971 Large-amplitude elongated-body theory of fish locomotion. *Proc. R. Soc. Lond. B* **179**, 125–138. (doi:10.1098/rspb.1971.0085)
32. Eloy C. 2013 On the best design for undulatory swimming. *J. Fluid Mech.* **717**, 48–89. (doi:10.1017/jfm.2012.561)
33. Eloy C, Kofman N, Schouveiler L. 2012 The origin of hysteresis in the flag instability. *J. Fluid Mech.* **691**, 583–593. (doi:10.1017/jfm.2011.494)
34. Nayfeh AH, Mook DT. 1995 *Nonlinear oscillations*. New York, NY: Wiley.
35. Nakashima M, Satou K, Miura Y. 2007 Development of swimming human simulation model considering rigid body dynamics and unsteady fluid force for whole body. *J. Fluid Sci. Technol.* **2**, 56–67. (doi:10.1299/jfst.2.56)
36. Yadykin Y, Tenetov V, Levin D. 2001 The flowinduced vibration of a flexible strip hanging vertically in a parallel flow part 1: temporal aeroelastic instability. *J. Fluids Struct.* **15**, 1167–1185. (doi:10.1006/jfls.2001.0400)
37. Eloy C, Souilliez C, Schouveiler L. 2007 Flutter of a rectangular plate. *J. Fluids Struct.* **23**, 904–919. (doi:10.1016/j.jfluidstructs.2007.02.002)
38. Doaré O, Sauzade M, Eloy C. 2011 Flutter of an elastic plate in a channel flow Confinement and finite-size effects. *J. Fluids Struct.* **27**, 76–88. (doi:10.1016/j.jfluidstructs.2010.09.002)
39. Shelley MJ, Zhang J. 2011 Flapping and bending bodies interacting with fluid flows. *Annu. Rev. Fluid Mech.* **43**, 449–465. (doi:10.1146/annurev-fluid-121108-145456)
40. Argentina M, Mahadevan L. 2005 Fluid-flow-induced flutter of a flag. *Proc. Natl Acad. Sci. USA* **102**, 1829–1834. (doi:10.1073/pnas.0408383102)
41. Tritton DJ. 1988 *Physical fluid dynamics*, 2nd edn. Oxford, UK: Clarendon Press.
42. Abbott IH. 1959 *Theory of wing sections: including a summary of airfoil data*. Mineola, NY: Dover Publications.
43. Ramananarivo S, Godoy-Diana R, Thiria B. 2011 Rather than resonance, flapping wing flyers may play on aerodynamics to improve performance. *Proc. Natl Acad. Sci. USA* **108**, 5964–5969. (doi:10.1073/pnas.1017910108)
44. Marais C, Thiria B, Wesfreid JE, Godoy- Diana R. 2012 Stabilizing effect of flexibility in the wake of a flapping foil. *J. Fluid Mech.* **710**, 659–669. (doi:10.1017/jfm.2012.390)
45. Zdravkovich MM. 1997 *Flow around circular cylinders,* vol. 1. *Fundamentals*. Oxford, UK: Oxford University Press.